

Toward Quantum-Aware Machine Learning: Improved Prediction of Quantum Dissipative Dynamics via Complex Valued Neural Networks

Muhammad Atif, Arif Ullah,^{a)} and Ming Yang^{b)}

School of Physics, Anhui University, Hefei, 230601, Anhui, China

(Dated: 8 January 2026)

Accurately modeling quantum dissipative dynamics remains challenging due to environmental complexity and non-Markovian memory effects. Although machine learning provides a promising alternative to conventional simulation techniques, most existing models employ real-valued neural networks (RVNNs) that inherently mismatch the complex-valued nature of quantum mechanics. By decoupling the real and imaginary parts of the density matrix, RVNNs can obscure essential amplitude–phase correlations, compromising physical consistency. Here, we introduce complex-valued neural networks (CVNNs) as a physics-consistent framework for learning quantum dissipative dynamics. CVNNs operate directly on complex-valued inputs, preserve the algebraic structure of quantum states, and naturally encode quantum coherences. Through numerical benchmarks on the spin-boson model and few variants of the Fenna–Matthews–Olson complex, we demonstrate that CVNNs outperform RVNNs in convergence speed, training stability, and physical fidelity—including significantly improved trace conservation and Hermiticity. These advantages increase with system size and coherence complexity, establishing CVNNs as a robust, scalable, quantum-aware classical approach for simulating open quantum systems in the pre-fault-tolerant quantum era.

I. INTRODUCTION

Open quantum systems provide a fundamental framework for understanding how quantum states evolve under the influence of external environments (baths). Such system–environment interactions are central to numerous physical phenomena, including quantum information processing¹, quantum memory², quantum transport³, photosynthetic energy transfer⁴, and biochemical processes such as proton tunneling in DNA⁵. Conceptually, in the system-bath model, an open quantum system consists of a primary subsystem of interest coupled to an external bath. The dynamics of the subsystem are encoded in the reduced density matrix (RDM), which captures both intrinsic quantum evolution and the influence of environmental degrees of freedom.

Modeling environmental effects, however, is highly challenging due to the vast and often continuous degrees of freedom associated with the bath. Existing approaches span two broad categories: mixed quantum–classical treatments and fully quantum formulations. Mixed quantum–classical schemes^{6–17} treat the system quantum mechanically while representing the environment through classical phase-space variables such as molecular vibrations or solvent motion, whose evolution follows Newtonian or Hamiltonian dynamics. This hybridization dramatically reduces computational cost by avoiding an explicit representation of the environment’s Hilbert space.

Fully quantum approaches, in contrast, place both the system and the environment within the quantum Hilbert space, enabling a complete treatment of coherence, dissipation, and entanglement. Path-integral-based

methods such as the hierarchical equations of motion (HEOM)^{18–25} and the quasiadiabatic propagator path integral (QUAPI)^{19,26} rigorously capture non-Markovian memory effects. Similarly, quantum master equation approaches—including the stochastic equation of motion (SEOM)^{27–32} and the generalized master equation^{33,34}—provide alternative fully quantum frameworks for describing environmental interactions.

Despite their success, both categories face well-known limitations. Mixed quantum–classical approaches may break detailed balance^{35–37} or fail to capture subtle quantum correlations³⁸. Fully quantum methods, while theoretically rigorous, often become prohibitively expensive for strong coupling regimes, long memory times, or large environmental modes, where fine temporal resolution is required to ensure numerical stability.

In response to these challenges, machine learning (ML) has recently emerged as a promising alternative for modeling complex spatiotemporal dynamics in quantum systems.^{39–65} Existing work, which rely exclusively on real-valued neural networks (RVNNs), have demonstrated strong predictive capabilities in forecasting quantum dynamics from the past history of the system and in learning direct mappings between system parameters, time, and the corresponding quantum states.

Despite these successes, a fundamental representational tension exists: quantum mechanics is intrinsically formulated within a complex-valued Hilbert space. This complex structure is not merely a mathematical convenience but encodes essential physical information, particularly in the phase relationships that define quantum coherence and interference. A parallel and compelling development across diverse scientific and engineering domains—from advanced signal processing and computational imaging to materials discovery and even emerging architectures for large language models^{66–77}—underscores that complex-valued

^{a)}Electronic mail: arif@ahu.edu.cn

^{b)}Electronic mail: mingyang@ahu.edu.cn

neural networks (CVNNs) possess a unique, intrinsic capacity to capture phase-dependent structures and continuous rotational symmetries. These are features that RVNNs, by their architectural design, inherently struggle to represent. The standard practice in RVNNs is to decouple the real and imaginary components of complex-valued data, processing them through separate, parallel real-valued pathways. This bifurcation risks discarding or obscuring the critical correlations that are holistically encoded within the complex geometry of quantum states, potentially limiting physical fidelity and generalization.

While quantum neural networks would, in principle, offer the most natural framework for quantum dynamics learning, current noisy intermediate-scale quantum (NISQ)-era devices remain too limited in scale and fidelity to outperform classical approaches. This motivates the search for classical architectures that can emulate essential quantum features without requiring quantum hardware. Given that complex numbers serve as a compact and faithful representation of quantum structure,^{66–68} CVNNs emerge as a promising intermediary between RVNNs and fully quantum models.

In this work, we conduct a systematic comparison between CVNNs and RVNNs for learning and forecasting quantum dissipative dynamics. Using the spin-boson (SB) model and several variants of the Fenna–Matthews–Olson (FMO) complex, we show that CVNNs converge faster, exhibit greater training stability, and yield predictions with improved physical fidelity—including superior trace conservation and Hermiticity—relative to RVNNs. Importantly, these advantages become increasingly pronounced with growing system size and coherence complexity, highlighting the scalability of the CVNN framework. Together, our results establish CVNNs as a powerful classical surrogate for quantum-aware learning and a practical pathway for modeling open quantum systems in the pre-fault-tolerant quantum era.

II. THEORY AND METHODOLOGY

We consider an open quantum system S with Hilbert space \mathcal{H}_S of dimension n , interacting with an environment E with Hilbert space \mathcal{H}_E of dimension d . The joint system $S + E$ evolves unitarily under the Liouville–von Neumann equation ($\hbar = 1$)

$$\dot{\rho}(t) = -i[H, \rho(t)], \quad (1)$$

where H is the total Hamiltonian acting on the tensor product space $\mathcal{H}_S \otimes \mathcal{H}_E$, and $\rho(t) \in \mathbb{C}^{(nd) \times (nd)}$ denotes the full density matrix of system plus environment. Given an initially factorized state

$$\rho(0) = \rho_S(0) \otimes \rho_E(0), \quad (2)$$

the unitary propagator $U(t) = e^{-iHt} \in \mathbb{C}^{(nd) \times (nd)}$ generates the reduced dynamics of the subsystem through the partial trace,

$$\rho_S(t) = \text{Tr}_E [U(t)\rho(0)U^\dagger(t)], \quad (3)$$

where $\rho_S(t) \in \mathbb{C}^{n \times n}$ represents the RDM of the system. The map $\rho_S(0) \mapsto \rho_S(t)$ is typically non-Markovian and cannot, in general, be expressed as a closed local evolution equation. Instead, one may write a generalized master equation of the form

$$\dot{\rho}_S(t) = -i[H_S, \rho_S(t)] + \mathcal{R} \left[\rho_S(s) \right]_{0 \leq s \leq t}, \quad (4)$$

where H_S acts on the system alone, and \mathcal{R} is a superoperator encoding dissipation, decoherence, and memory. Abstractly, the reduced dynamics can therefore be represented as a history-dependent quantum map

$$\rho_S(t) = \Phi_t [\{\rho_S(s)\}_{0 \leq s < t}], \quad (5)$$

where Φ_t is, in principle, a completely positive and trace-preserving (CPTP) operator-valued functional on the space of continuous matrix-valued trajectories.

From ML perspective, the goal is to learn and approximate the non-Markovian evolution operator Φ_t using a parametrized model. To formalize this, let $\rho_S(t_{k-k'}), \dots, \rho_S(t_k) \subset \mathbb{C}^{n \times n}$ denote a discrete-time history window of length $k' + 1$, containing the most recent RDMs. We define a recursive operator

$$\mathcal{C}_{\text{rec}} : (\mathbb{C}^{n \times n})^{k'+1} \longrightarrow (\mathbb{C}^{n \times n})^N \quad (6)$$

which maps the sequence of past RDMs to the next N future RDMs,

$$\mathcal{C}_{\text{rec}}(\rho_S(t_{k-k'}), \dots, \rho_S(t_k)) = (\rho_S(t_{k+1}), \dots, \rho_S(t_{k+N})). \quad (7)$$

Formally, if we denote the discrete trajectory at step k by the vector-valued sequence

$$\mathbf{R}_k = (\rho_S(t_{k-k'}), \dots, \rho_S(t_k)) \in (\mathbb{C}^{n \times n})^{k'+1}, \quad (8)$$

then the recursion reads

$$\begin{aligned} \mathbf{R}_{k+N} &= (\rho_S(t_{k-k'+N+1}), \dots, \rho_S(t_{k+N})) \\ &= \text{shift}_N(\mathbf{R}_k, \mathcal{C}_{\text{rec}}(\mathbf{R}_k)), \end{aligned} \quad (9)$$

where shift_N discards the oldest N matrices and appends the newly predicted ones. Iterating this mapping produces the full predicted trajectory of the reduced dynamics $\rho_S(t_0), \rho_S(t_1), \dots, \rho_S(t_T)$ providing a recursive ML-based approximation of the true non-Markovian propagator Φ_t over the time interval of interest.

A. Real and complex valued neural networks

To implement the recursive operator \mathcal{C}_{rec} we employ both RVNNs and CVNNs. Let $\rho_S(t) \in \mathbb{C}^{n \times n}$ denote the RDM of the system. Because ρ_S is Hermitian ($\rho_{kl} = \rho_{lk}^*$), all independent information resides in the upper-triangular part including the diagonal; we denote this vectorized object by $\rho_S^{\text{up}} \in \mathbb{C}^{n(n+1)/2}$. Using the upper-triangular representation reduces input dimensionality

and enforces Hermiticity by construction (the lower triangle is recovered by conjugation).

In the RVNN formulation, all inputs, weights, and activations lie in \mathbb{R} , requiring a real decomposition of the complex-valued upper-triangular data. For each off-diagonal element $\rho_{kl} = a_{kl} + ib_{kl}$ with $k < l$, the real and imaginary components a_{kl}, b_{kl} are treated as separate degrees of freedom, while diagonal entries—being real and having no imaginary component—contribute only their real values. Flattening this representation yields a real vector $\mathbf{x}^{\text{up}} \in \mathbb{R}^{n^2}$. An RVNN layer then performs the mapping

$$\mathbf{y} = \sigma(\mathbf{W}\mathbf{x}^{\text{up}} + \mathbf{b}), \quad \mathbf{W} \in \mathbb{R}^{m \times n^2}, \quad \mathbf{b} \in \mathbb{R}^m, \quad (10)$$

with σ a real-valued nonlinearity (ReLU, tanh, etc.). This real embedding treats Re and Im components as independent channels and therefore lacks the natural complex geometry: real multiplication effects independent scaling of each channel but cannot implement planar rotations or amplitude–phase coupling in a single algebraic operation. Consequently RVNNs are not \mathbb{C} -linear and do not preserve phase structure; they learn dynamics in a surrogate real vector space rather than the native complex Hilbert space, which can limit expressivity for long-time coherent phenomena.

CVNNs, in contrast, operate directly on complex-valued inputs and preserve the algebraic structure of complex state evolution. We encode the upper-triangular RDM directly as a complex vector $\mathbf{z} = \rho_S^{\text{up}} \in \mathbb{C}^{n(n+1)/2}$. For diagonal entries, which are purely real, we embed them uniformly into \mathbb{C} by mapping $a \mapsto a + ia$ at the input; at the output, this additive phase is discarded to maintain Hermiticity. A CVNN layer computes

$$\mathbf{f}_{\mathbb{C}}(\mathbf{z}) = \sigma_{\mathbb{C}}(\mathbf{W}\mathbf{z} + \mathbf{b}), \quad \mathbf{W} \in \mathbb{C}^{m \times n(n+1)/2}, \quad \mathbf{b} \in \mathbb{C}^m, \quad (11)$$

where $\sigma_{\mathbb{C}}$ is a complex-valued activation applied component-wise. Writing $\mathbf{z} = \mathbf{u} + i\mathbf{v}$, $\mathbf{W} = \mathbf{W}_r + i\mathbf{W}_i$ and $\mathbf{b} = \mathbf{b}_r + i\mathbf{b}_i$, the linear part is represented in real block form as

$$\begin{bmatrix} \text{Re}(\mathbf{W}\mathbf{z} + \mathbf{b}) \\ \text{Im}(\mathbf{W}\mathbf{z} + \mathbf{b}) \end{bmatrix} = \begin{bmatrix} \mathbf{W}_r & -\mathbf{W}_i \\ \mathbf{W}_i & \mathbf{W}_r \end{bmatrix} \begin{bmatrix} \mathbf{u} \\ \mathbf{v} \end{bmatrix} + \begin{bmatrix} \mathbf{b}_r \\ \mathbf{b}_i \end{bmatrix}. \quad (12)$$

This structured block matrix represents true complex multiplication, where the real and imaginary parts transform jointly rather than independently, preserving amplitude–phase coupling before the activation is applied.

Geometrically, each component of ρ_S^{up} , say $\rho_{kl} = u_{kl} + iv_{kl}$, corresponds to a two-dimensional vector (u_{kl}, v_{kl}) in the complex plane. Multiplication by a complex weight $W_{kl}^c = W_{kl}^r + iW_{kl}^i$ performs a rotation and a scaling in this plane: the angle of rotation is

$$\arg(W_{kl}^c) = \arctan(W_{kl}^i/W_{kl}^r), \quad (13)$$

and the magnitude,

$$|W_{kl}^c| = \sqrt{(W_{kl}^r)^2 + (W_{kl}^i)^2}, \quad (14)$$

determines the dilation (scaling). Adding a complex bias translates the vector in the same plane. Thus, each CVNN neuron implements a transformation that simultaneously rotates, scales, and translates the complex-valued entries of the RDM—precisely the class of planar transformations compatible with complex linearity. No RVNN can generate such rotations in a single step, because real weights act independently on Re and Im channels and therefore cannot encode angle-preserving transformations. This geometric capacity to preserve and manipulate phase relationships is precisely why CVNNs are more faithful to reproduce phase-sensitive, interference-driven, and non-Markovian quantum dynamics.

B. Weight initialization in real-valued and complex-valued neural layers

Accurate modeling of quantum dynamical maps such as the recursive operator \mathcal{C}_{rec} requires careful control over signal propagation in both real-valued and complex-valued neural architectures. Because RVNNs operate in \mathbb{R}^d whereas CVNNs operate in \mathbb{C}^d , their initialization schemes must be adapted to the geometry and variance structure of these two spaces. The real and imaginary channels in a CVNN jointly determine the magnitude and phase of the signal, so the initialization must preserve neutrality in the complex plane while matching the variance of the underlying real-valued baseline.

In RVNN, we initialize each weight using the He (Kaiming) uniform distribution⁷⁸ with variance $\text{Var}[W_{kl}] = 2/n_{\text{in}}$ with n_{in} as a number of input features. We compute the standard deviation $\sigma = \sqrt{2/n_{\text{in}}}$ and sample from a symmetric uniform distribution $[-a, a]$ where $a = \sqrt{3}\sigma$. Since a uniform distribution on $[-a, a]$ has variance $a^2/3$, this ensures the outgoing variance matches the desired He level. Because the recursive operator repeatedly applies real-valued linear maps followed by nonlinearities, this initialization keeps the forward signal variance approximately stable and prevents vanishing gradients in early training. All real-valued biases are initialized to zero, a standard practice that allows the nonlinearities to determine the initial operating point.

The complex-valued layers in a CVNN require a different treatment because a complex weight $W_{kl} = W_{kl}^r + iW_{kl}^i$ is effectively a 2D vector whose variance decomposes across two components. If both real and imaginary parts were initialized with the real He variance $2/n_{\text{in}}$, the effective complex variance $\mathbb{E}|W_{kl}|^2 = \text{Var}[W_{kl}^r] + \text{Var}[W_{kl}^i]$ would double, leading to unstable magnitude growth.⁷² To avoid this, we assign each component the reduced variance $\text{Var}[W_{kl}^r] = \text{Var}[W_{kl}^i] = 1/n_{\text{in}}$. The resulting complex variance is then

$$\mathbb{E}|W_{kl}|^2 = \frac{1}{n_{\text{in}}} + \frac{1}{n_{\text{in}}} = \frac{2}{n_{\text{in}}}, \quad (15)$$

matching the real He initialization only after combining the two channels. We achieve this by setting $\sigma = \sqrt{1/n_{\text{in}}}$

and sampling W_{kl}^r and W_{kl}^i independently from a uniform distribution on $[-a, a]$ with $a = \sqrt{3}\sigma$. This construction preserves phase neutrality: the distribution of W_{kl} has no preferred direction in the complex plane, ensuring no initial bias in rotational transformations. Such neutrality is critical for maintaining phase coherence, because the linear operator induced by a complex weight, $z \mapsto W_{kl} z = (W_{kl}^r + iW_{kl}^i)(u_{kl} + iv_{kl})$, corresponds to a rotation by $\arg(W_{kl})$ and a scaling by $|W_{kl}|$. Any imbalance in the initial variances of W_{kl}^r and W_{kl}^i would distort this geometry, bias the angular distribution, or amplify certain directions in the complex plane. By splitting the variance equally between the two channels, the magnitude distribution remains normalized and the initial transformations act as unbiased complex scalings and rotations. Coming to Biases, in CVNN implementation, we set both the real and imaginary parts to zero, ensuring that the early-stage operator acts without translation, consistent with the affine-free structure of quantum channels.

III. SYSTEMS OF INTEREST

To evaluate the efficiency and quantum-awareness of RVNNs and CVNNs, we benchmark both architectures on representative open quantum systems that capture essential features of coherent evolution, dissipation, and system–bath interactions. Our first testbed is the paradigmatic SB model, which describes a two-level quantum system (qubit) interacting with a bosonic environment composed of infinitely many harmonic modes. The composite Hamiltonian is

$$\mathbf{H} = \varepsilon \sigma_z + \Delta \sigma_x + \sum_k \omega_k b_k^\dagger b_k + \sigma_z \sum_k c_k (b_k^\dagger + b_k), \quad (16)$$

where ε denotes the energy splitting of the two-level system, Δ is the tunneling amplitude between states, and σ_z, σ_x are Pauli matrices. The bosonic bath is defined through harmonic-mode operators b_k, b_k^\dagger with mode frequencies ω_k , coupled to the system with strength c_k . Environmental influence is encoded via the Debye spectral density,

$$J(\omega) = 2\lambda \frac{\gamma\omega}{\omega^2 + \gamma^2}, \quad (17)$$

which introduces a reorganization energy λ and a characteristic environmental relaxation timescale $\tau = 1/\gamma$.

As a complementary and more structurally complex system, we also consider the FMO complex, a pigment–protein complex central to energy transfer in green sulfur bacteria. Each monomer of the FMO trimer contains seven or eight bacteriochlorophyll sites, forming a network through which electronic excitations propagate with remarkably high efficiency. The dynamics are mod-

eled using the Frenkel exciton Hamiltonian,

$$\begin{aligned} \mathbf{H} = & \sum_{n=1}^N |n\rangle \varepsilon_n \langle n| + \sum_{n \neq m} |n\rangle J_{nm} \langle m| \\ & + \sum_{n,k} \left(\frac{1}{2} P_{k,n}^2 + \frac{1}{2} \omega_{k,n}^2 Q_{k,n}^2 \right) I \\ & - \sum_{n,k} |n\rangle c_{k,n} Q_{k,n} \langle n| + \sum_n |n\rangle \lambda_n \langle n|. \end{aligned} \quad (18)$$

Here, ε_n denotes the site energy, J_{nm} the electronic coupling between sites, and $Q_{k,n}$, $P_{k,n}$, and $\omega_{k,n}$ describe the coordinate, momentum, and frequency of environmental modes coupled to site n with strength $c_{k,n}$. The reorganization energy λ_n accounts for environmentally induced shifts in site energies and I is the identity matrix for dimensional compatibility. For consistency and physical relevance, the environmental spectral density is again taken to be Debye with identical parameters across all sites.

IV. RESULTS AND DISCUSSION

In this work, we benchmark the performance of CVNNs against their real-valued counterparts (RVNNs) across four representative quantum dynamical systems of increasing Hilbert-space dimension: (i) the SB model, (ii) a hypothetical 4-site FMO model describing the population dynamics of the first four bacteriochlorophyll (BChl) sites of a 7-site FMO complex, (iii) the full 7-site FMO complex, and (iv) an 8-site extension of the FMO system. This systematic variation in system size allows us to assess the scalability and representational advantages of CVNNs relative to RVNNs.

For each system, we independently trained two neural network models—a RVNN and a CVNN—using identical training data. Both models adopt a fully connected sequence-to-sequence architecture consisting of five layers: one input layer, three hidden layers, and one output layer. In the RVNN, all layers employ real-valued weights and biases together with the ReLU activation function. In contrast, the CVNN is constructed using custom complex-valued linear layers with complex weights and biases, combined with a complex ReLU (CReLU) activation function that applies the ReLU operation separately to the real and imaginary components. To ensure a fair comparison, the total number of trainable parameters in the CVNN and RVNN architectures is kept approximately the same. Moreover, both network architectures are implemented from scratch within the PyTorch framework, allowing full control over the operations. A schematic overview of the training and optimization workflow for both models is shown in Fig. 1.

To guarantee that the predicted RDMs satisfy the fundamental physical constraints of quantum mechanics—namely trace conservation, positive semi-definiteness, and bounded eigenvalues—we employ a

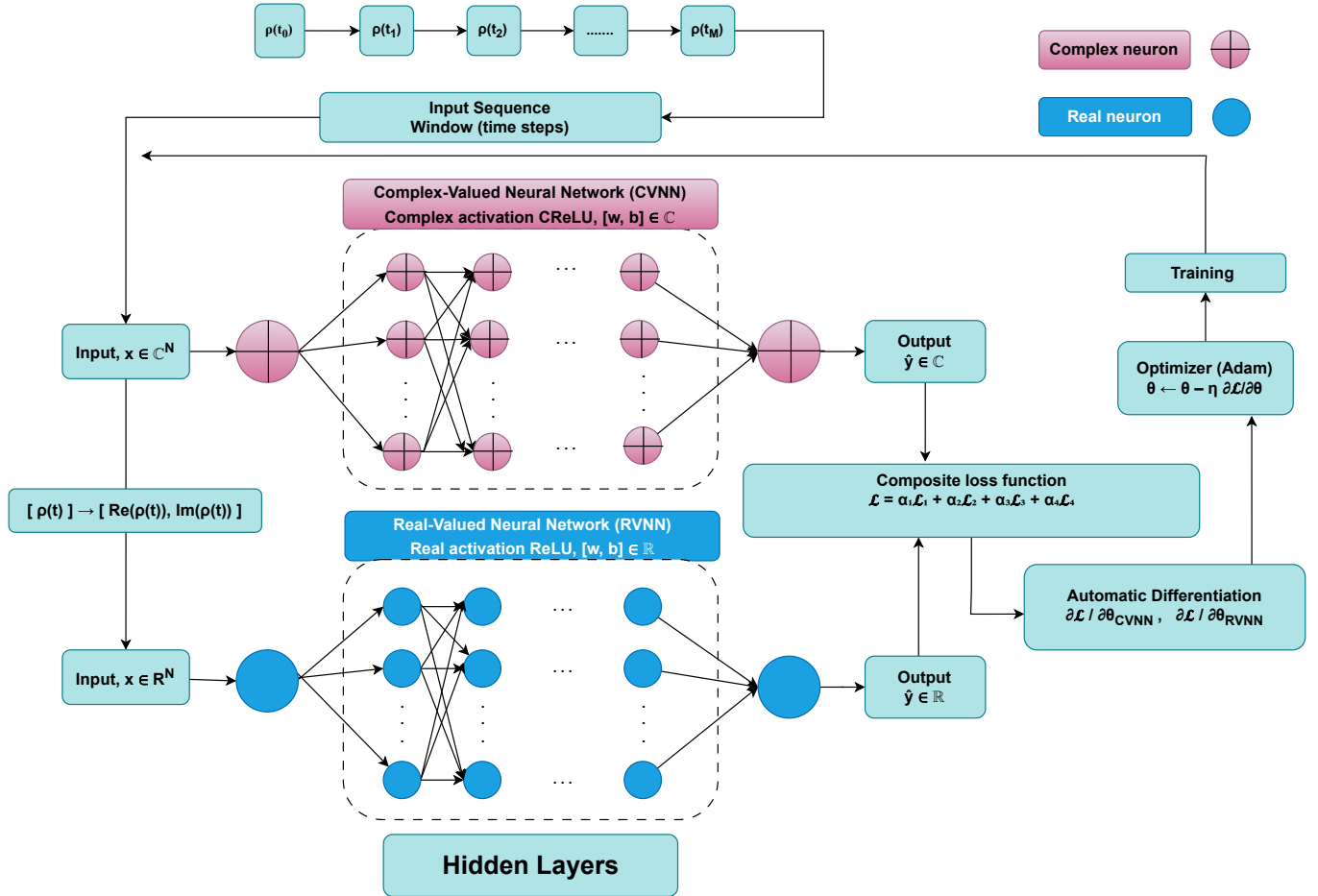


FIG. 1. A schematic flowchart illustrating the general training process for both CVNN and RVNN models.

composite loss function of the form

$$\mathcal{L} = \alpha_1 \mathcal{L}_1 + \alpha_2 \mathcal{L}_2 + \alpha_3 \mathcal{L}_3 + \alpha_4 \mathcal{L}_4, \quad (19)$$

where each term enforces a specific physical or numerical requirement.

The primary accuracy term, \mathcal{L}_1 , is defined as the mean squared error (MSE) between the predicted RDM elements $\rho_S(t)$ and the corresponding reference values $\tilde{\rho}_S(t)$,

$$\mathcal{L}_1 = \frac{1}{N_t \cdot n^2} \sum_{t=1}^{N_t} \sum_{i,j=1}^n (\tilde{\rho}_{S,ij}(t) - \rho_{S,ij}(t))^2, \quad (20)$$

where N_t denotes the total number of time steps and n is the dimension of the system Hilbert space.

Trace preservation of the density matrix is enforced through the penalty term

$$\mathcal{L}_2 = \frac{1}{N_t} \sum_{t=1}^{N_t} (\text{Tr} \rho_S(t) - 1)^2, \quad (21)$$

which penalizes deviations of the predicted trace from unity at each time step.

The positive semi-definiteness of the RDM is imposed by penalizing negative eigenvalues $\mu_i(t)$ via

$$\mathcal{L}_3 = \frac{1}{N_t \cdot n} \sum_{t=1}^{N_t} \sum_{i=1}^n \max(0, -\mu_i(t))^2. \quad (22)$$

In addition, physically admissible density matrices require all eigenvalues to lie within the interval $[0, 1]$. This constraint is enforced through

$$\mathcal{L}_4 = \frac{1}{N_t \cdot n} \sum_{t=1}^{N_t} \sum_{i=1}^n (\text{clip}(\mu_i(t), 0, 1) - \mu_i(t))^2, \quad (23)$$

where the clipping operation is defined as

$$\text{clip}(\mu_i(t), 0, 1) = \begin{cases} 0, & \mu_i(t) < 0, \\ \mu_i(t), & 0 \leq \mu_i(t) \leq 1, \\ 1, & \mu_i(t) > 1. \end{cases} \quad (24)$$

The relative importance of each constraint is controlled by the weighting coefficients $\alpha_1 - \alpha_4$. In all simulations reported here, we use $\alpha_1 = \alpha_2 = 1.0$, $\alpha_3 = 2.0$, and $\alpha_4 = 3.0$. Collectively, the loss terms $\mathcal{L}_1 - \mathcal{L}_4$ ensure accurate

TABLE I. MAE in trace conservation, averaged over 100 trajectories, for RDMs predicted by CVNN and RVNN. The MAE measures the average deviation of the predicted trace from its theoretical value of 1.

Model	CVNN (MAE)	RVNN (MAE)
SB Model	2.92e-05	3.15e-05
4-site FMO complex	6.30e-05	7.21e-04
7-site FMO complex	4.02e-05	6.36e-05
8-site FMO complex	4.98e-05	5.33e-05

reproduction of the reference dynamics while rigorously enforcing the fundamental physical properties of RDMs.

To train and evaluate the proposed neural network models, we employ high-quality reference data generated using numerically exact or well-established open quantum system approaches. For the SB model, training data are obtained from the openly accessible QD3SET-1 database⁷⁹. The dataset spans a four-dimensional parameter space, denoted by \mathcal{D}_{sb} , defined by the normalized system-bath parameters ($\varepsilon/\Delta, \lambda/\Delta, \gamma/\Delta, \beta\Delta$), which respectively characterize the bias-to-tunneling ratio, bath reorganization energy, bath relaxation rate, and inverse temperature. In total, \mathcal{D}_{sb} comprises 1000 independent simulations, with 500 trajectories for the symmetric case and 500 for the asymmetric case. For each parameter combination, the RDM dynamics are computed using the HEOM formalism^{18,23,80,81}, ensuring numerically accurate reference trajectories.

For the 7-site and 8-site FMO complexes, training data are likewise sourced from the QD3SET-1 database. These datasets describe excitation energy transfer dynamics initiated at site 1 and site 6 for the 7-site complex, with site 8 additionally included for the 8-site system. The associated parameter space (λ, γ, T) spans bath reorganization energy, relaxation rate, and temperature, yielding a total of 500 simulations for each initial excitation scenario. The quantum dynamics are propagated using a trace-conserving local thermalizing Lindblad master equation (LTLME)⁸². The system Hamiltonians are parameterized following the models of Adolfs and Renger for the 7-site FMO complex⁸³ and Jia *et al.* for the 8-site extension⁸⁴.

Since a 4-site FMO model is not available in the QD3SET-1 database, we generate the corresponding dataset independently using the same LTLME framework and bath parameters as employed for the 7-site FMO complex, with the dynamics initialized by an excitation localized on site 1. This construction ensures consistency across all FMO prototypes considered in this study.

To improve training efficiency and ensure representative coverage of the parameter space, farthest point sampling^{41,85} is employed to select a subset of trajectories from each dataset. For the SB model, we consider only the symmetric case, comprising 500 trajectories from \mathcal{D}_{sb} . For each of the four systems—the SB model and the three FMO prototypes—we then select 400 trajectories for training via farthest point sampling, with the

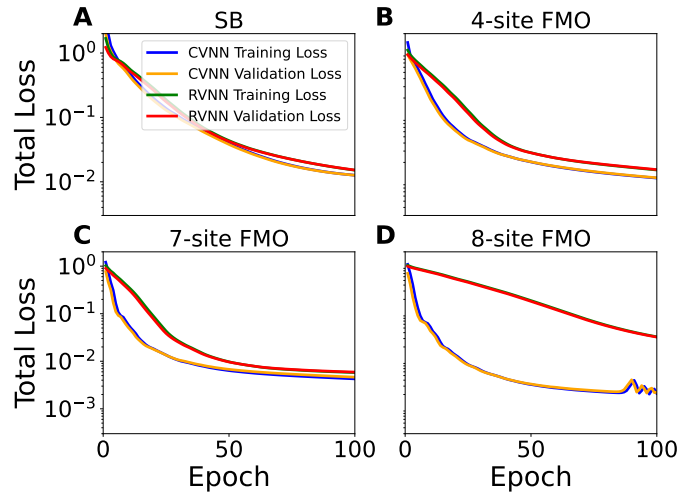


FIG. 2. A comparison of training and validation loss curves versus epoch number for the CVNN and RVNN models. Results are shown for the SB model and all three prototypes of the FMO complex.

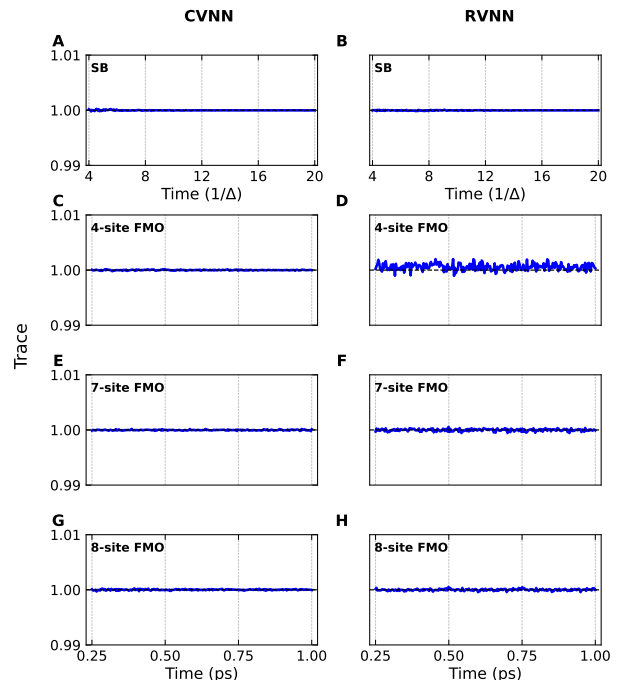


FIG. 3. Comparison of trace conservation in predicted dissipative dynamics. Results for the CVNN (left) and RVNN (right) are shown for, from top to bottom, the SB model and the 4-site, 7-site, and 8-site FMO complexes. All predictions correspond to trajectories not seen during training. Parameters are: SB model— $\varepsilon/\Delta = 0.0, \gamma/\Delta = 9.0, \lambda/\Delta = 6.0, \beta\Delta = 1.0$; FMO complexes—4-site ($\gamma = 250 \text{ cm}^{-1}, \lambda = 70 \text{ cm}^{-1}, T = 130 \text{ K}$), 7-site ($\gamma = 350 \text{ cm}^{-1}, \lambda = 70 \text{ cm}^{-1}, T = 30 \text{ K}$), and 8-site ($\gamma = 400 \text{ cm}^{-1}, \lambda = 250 \text{ cm}^{-1}, T = 30 \text{ K}$).

remaining trajectories reserved for out-of-sample testing.

For the SB model, each trajectory spans a total duration of $20/\Delta$ with a time step of $dt = 0.05$. In contrast, the FMO dynamics is restricted to a total time of 2 ps with a time step of 0.005 ps. During training, both RVNN and CVNN models operate in a sequence-to-sequence forecasting mode, wherein a fixed-length history of RDMs is provided as input and multiple future time steps are predicted simultaneously in a single forward pass (“one-shot” prediction). Specifically, for the SB model, each training sample consists of 81 input time steps, and the network is trained to predict the subsequent 40 time steps. For the 4-site, 7-site, and 8-site FMO complexes, each training sample likewise contains 81 input time steps, with the models trained to predict the next 80 time steps.

All RVNN and CVNN models are trained for 10^5 epochs using the Adam optimizer with a learning rate of 10^{-3} . This unified training protocol enables a controlled and systematic comparison of the predictive accuracy and physical consistency of real- and complex-valued neural network architectures across quantum systems of increasing complexity.

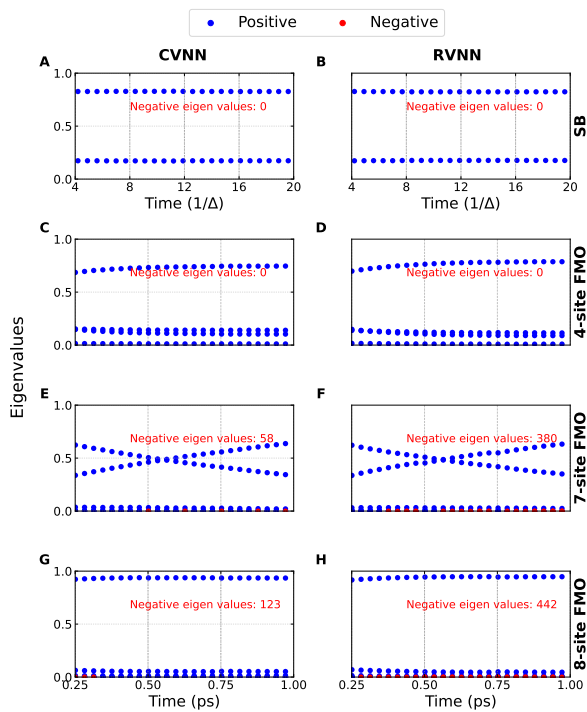


FIG. 4. Evaluation of positive semi-definiteness of predicted RDMs via eigenvalue spectra for CVNN and RVNN models across all considered systems. Sparse positive eigenvalues are shown as blue dots for clarity, while negative eigenvalues are indicated in red, with their counts labeled for each model and system. Simulation parameters are consistent with those in Fig. 3.

As an initial step in comparing the two architectures, we assess the learning performance of the CVNN

and RVNN by examining their training and validation loss evolution across the considered quantum systems (Fig. 2). Analysis of the first 100 training epochs—a regime where key differences in learning efficiency emerge—reveals that both models exhibit a rapid initial loss decrease. For the low-dimensional SB model, where coherent effects are minimal, the CVNN and RVNN show nearly identical loss trajectories, reflecting the limited dynamical role of complex off-diagonal terms in the RDM.

This performance divergence intensifies with system size. For the 4- and 7-site FMO prototypes, the CVNN achieves a consistently faster reduction in both training and validation loss compared to the RVNN. This advantage is most pronounced for the largest, coherence-rich 8-site FMO complex, where the CVNN exhibits a substantially more rapid loss decrease. These results demonstrate that the CVNN’s superior learning efficiency scales with system size, directly correlating with the increasing number and dynamical importance of complex-valued off-diagonal RDM elements.

We now turn to the physical fidelity of the predicted RDMs. We first assess trace conservation by comparing the CVNN and RVNN predictions. Figure 3 shows the trace evolution for a representative test trajectory, while Table I reports the mean absolute error (MAE) of the trace relative to unity, averaged over 100 trajectories.

TABLE II. Average negative eigenvalues calculated over 100 independent trajectories per model.

Model	CVNN	RVNN
SB Model	0.0	0.0
4-site FMO complex	39.46	43.23
7-site FMO complex	40.33	71.36
8-site FMO complex	57.43	62.69

For the low-dimensional SB model, both CVNN and RVNN exhibit nearly identical trace behavior in the single-trajectory example and comparable ensemble-averaged MAEs on the order of 10^{-5} . As shown in Table I, clear differences emerge for the FMO systems. In the 4-site FMO complex, the CVNN achieves substantially lower trace error than the RVNN, with the latter displaying an order-of-magnitude larger deviation. For the 7-site and 8-site FMO complexes, both models maintain trace errors in the 10^{-5} range; however, the CVNN consistently yields slightly smaller MAEs.

We next evaluate positive semi-definiteness by analyzing the eigenvalue spectra of the predicted RDMs. Representative single-trajectory results are shown in Fig. 4, and ensemble-averaged statistics over 100 trajectories are summarized in Table II.

For the SB model, both CVNN and RVNN preserve positive semi-definiteness in all predictions, with no negative eigenvalues observed in either the single-trajectory spectra or the ensemble-averaged statistics. A similar level of consistency is found for the 4-site FMO complex, where both models exhibit only a small number of neg-

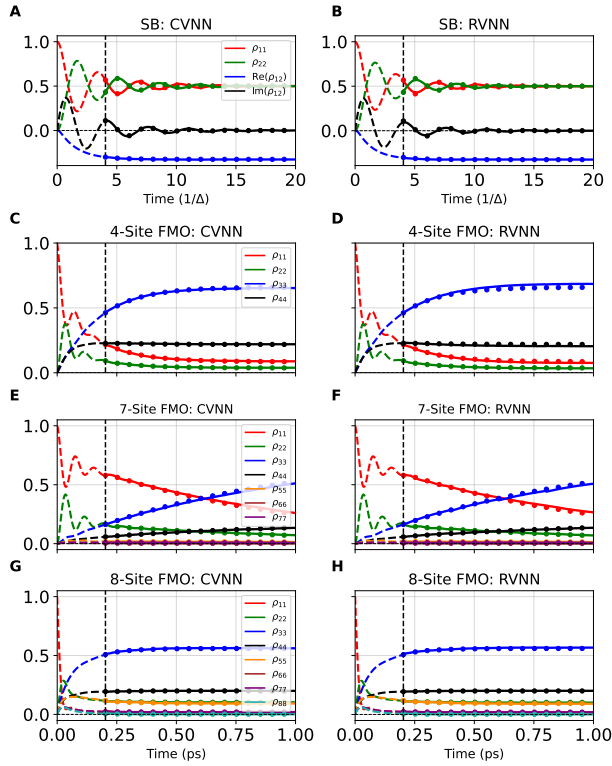


FIG. 5. Predicted time evolution of RDM elements. Panels (A, C, E, G) show CVNN results and panels (B, D, F, H) show RVNN results for the following systems: (A, B) SB model (populations and coherences); (C, D) populations of the 4-site FMO complex; (E, F) populations of the 7-site FMO complex; (G, H) populations of the 8-site FMO complex. Reference data are shown as dots. A vertical dashed line in each panel separates the provided input dynamics from the predicted dynamics. Coherence evolution for the FMO complexes is provided in the Supporting Information. Simulation parameters match those in Fig. 3.

TABLE III. MAE for predicted RDM elements. For each model and system, the MAE (averaged over 100 trajectories and across all time steps) is reported separately for the diagonal elements and for the off-diagonal elements (calculated as the mean of the MAE for the real and imaginary components).

Model	CVNN		RVNN	
	Diag	Off-diag (Real, Imag)	Diag	Off-diag (Real, Imag)
SB model	6.03e-4 (1.91e-3, 5.26e-4)		7.85e-4 (1.95e-3, 6.55e-4)	
4-site FMO	1.52e-3 (9.16e-4, 7.60e-5)		2.75e-3 (1.80e-3, 2.12e-4)	
7-site FMO	6.29e-4 (5.28e-4, 6.56e-5)		1.23e-3 (1.01e-3, 9.24e-5)	
8-site FMO	5.13e-4 (6.98e-4, 6.07e-5)		5.78e-4 (8.08e-4, 7.82e-5)	

ative eigenvalues on average, with the CVNN showing a modest but systematic reduction relative to the RVNN.

As the system size increases, however, more pronounced differences emerge. For the 7-site and 8-site FMO complexes, violations of positive semi-definiteness become more frequent, reflecting the increased complexity and coherence of the dynamics. For these systems,

CVNN consistently produces fewer negative eigenvalues than the RVNN, both in the representative eigenvalue spectra shown in Fig. 4 and in the ensemble-averaged results summarized in Table II. In particular, the average number of negative eigenvalues is reduced by nearly a factor of two for the 7-site system and remains systematically lower for the 8-site complex.

Taken together, the trace and eigenvalue analyses demonstrate that CVNNs preserve fundamental physical constraints at least as accurately as RVNNs, and in several cases significantly better. This improved physical consistency correlates with the enhanced learning efficiency observed in Fig. 2, highlighting the advantage of operating natively in the complex domain for modeling larger and more coherent open quantum systems.

To further evaluate the CVNN and RVNN models, we compare their predictive accuracy for RDM dynamics. Figure 5 shows the time evolution of diagonal (population) and off-diagonal (coherence) elements for a representative test trajectory. For clarity, both diagonal and off-diagonal elements are shown for the SB model, while for the FMO complexes the off-diagonal dynamics are provided in the Supporting Information. Ensemble-averaged accuracy is quantified in Table III, which reports the MAE averaged over 100 independent test trajectories and all time steps, separately for diagonal and off-diagonal RDM elements.

For the SB model, both architectures achieve comparable accuracy for populations and coherences, consistent with the relatively simple dynamics and the limited role of long-lived quantum coherence. As system size increases, systematic differences emerge. For the 4-site and 7-site FMO complexes, the CVNN consistently yields lower MAEs than the RVNN for both diagonal and off-diagonal elements, with particularly pronounced improvements in the coherences. In the 7-site FMO case, this enhanced accuracy correlates with the CVNN's superior preservation of positive semi-definiteness, as evidenced by the reduced number of negative eigenvalues reported in Table II.

For the 8-site FMO complex, both models achieve similar accuracy for the population dynamics, while the CVNN maintains a modest but systematic advantage in predicting off-diagonal elements. Notably, despite comparable MAEs, the RVNN exhibits larger violations of trace conservation and positive semi-definiteness for this system, highlighting that numerical accuracy alone does not guarantee physical fidelity.

Overall, these results demonstrate that CVNNs not only match or exceed RVNNs in predictive accuracy but also offer improved robustness with respect to fundamental quantum constraints, particularly as system size and coherence complexity increase.

V. CONCLUDING REMARKS

This work demonstrates that aligning ML architectures with the inherent mathematical structure of the physical systems they model is critical for performance. Quantum dissipative dynamics is fundamentally complex-valued, with essential information encoded in coupled amplitude-phase relationships and quantum coherences. Our results establish that neural networks operating natively in the complex domain offer a more natural and effective framework for learning such dynamics than conventional real-valued architectures, leading to superior accuracy and physical consistency.

In principle, quantum neural networks would provide the most faithful representation of quantum evolution. However, current NISQ hardware remains too constrained to offer practical advantages for this task. This limitation underscores the need for classical models that can capture essential quantum features without relying on quantum hardware. In this context, CVNNs emerge as a compelling intermediate paradigm—bridging the gap between purely real-valued models and fully quantum approaches.

By directly preserving the algebraic structure of complex-valued quantum states, CVNNs enable richer and more physically constrained representations. This translates to enhanced learning efficiency, greater stability with increasing system size, and more accurate adherence to quantum constraints as coherence complexity grows. More broadly, our findings position complex-valued ML as a promising and scalable direction for quantum-aware classical computation. It provides a hardware-independent pathway for modeling open quantum dynamics and can serve as an informative precursor to future hybrid classical–quantum strategies.

VI. ACKNOWLEDGMENTS

A.U. acknowledges funding from the National Natural Science Foundation of China (No. W2433037) and the Natural Science Foundation of Anhui Province (No. 2408085QA002).

VII. DATA AVAILABILITY

The code and data supporting this work are available at <https://github.com/Arif-PhyChem/cvnn>.

VIII. COMPETING INTERESTS

The authors declare no competing interests.

REFERENCES

- ¹Breuer HP, Laine EM, Piilo J, Vacchini B. Colloquium: Non-Markovian dynamics in open quantum systems. *Reviews of Modern Physics*. 2016;88(2):021002.
- ²Khodjasteh K, Sastrawan J, Hayes D, Green TJ, Biercuk MJ, Viola L. Designing a practical high-fidelity long-time quantum memory. *Nature Communications*. 2013;4(1):2045.
- ³Cui P, Li XQ, Shao J, Yan Y. Quantum transport from the perspective of quantum open systems. *Physics Letters A*. 2006;357(6):449-53.
- ⁴Zerah Harush E, Dubi Y. Do photosynthetic complexes use quantum coherence to increase their efficiency? Probably not. *Science advances*. 2021;7(8):eabc4631.
- ⁵Slocombe L, Sacchi M, Al-Khalili J. An open quantum systems approach to proton tunnelling in DNA. *Communications Physics*. 2022;5(1):109.
- ⁶Miller WH. The Semiclassical Initial Value Representation: A Potentially Practical Way for Adding Quantum Effects to Classical Molecular Dynamics Simulations. *The Journal of Physical Chemistry A*. 2001;105(13):2942-55.
- ⁷Cotton SJ, Miller WH. Symmetrical windowing for quantum states in quasi-classical trajectory simulations: Application to electronically non-adiabatic processes. *The Journal of chemical physics*. 2013;139(23).
- ⁸Liu J, He X, Wu B. Unified formulation of phase space mapping approaches for nonadiabatic quantum dynamics. *Accounts of chemical research*. 2021;54(23):4215-28.
- ⁹Runeson JE, Richardson JO. Spin-mapping approach for nonadiabatic molecular dynamics. *The Journal of Chemical Physics*. 2019;151(4):044119.
- ¹⁰Runeson JE, Richardson JO. Generalized spin mapping for quantum-classical dynamics. *The Journal of chemical physics*. 2020;152(8).
- ¹¹Mannouch JR, Richardson JO. A partially linearized spin-mapping approach for nonadiabatic dynamics. I. Derivation of the theory. *The Journal of chemical physics*. 2020;153(19).
- ¹²Mannouch JR, Richardson JO. A partially linearized spin-mapping approach for nonadiabatic dynamics. II. Analysis and comparison with related approaches. *The Journal of chemical physics*. 2020;153(19).
- ¹³Mannouch JR, Richardson JO. A partially linearized spin-mapping approach for simulating nonlinear optical spectra. *The Journal of Chemical Physics*. 2022;156(2).
- ¹⁴Tao G. A multi-state trajectory method for non-adiabatic dynamics simulations. *The Journal of Chemical Physics*. 2016;144(9).
- ¹⁵Mannouch JR, Richardson JO. A mapping approach to surface hopping. *The Journal of Chemical Physics*. 2023;158(10).
- ¹⁶Crespo-Otero R, Barbatti M. Recent advances and perspectives on nonadiabatic mixed quantum-classical dynamics. *Chemical reviews*. 2018;118(15):7026-68.
- ¹⁷Qiu J, Lu Y, Wang L. Multilayer subsystem surface hopping method for large-scale nonadiabatic dynamics simulation with hundreds of thousands of states. *Journal of Chemical Theory and Computation*. 2022;18(5):2803-15.
- ¹⁸Tanimura Y, Kubo R. Time evolution of a quantum system in contact with a nearly Gaussian-Markoffian noise bath. *Journal of the Physical Society of Japan*. 1989;58(1):101-14.
- ¹⁹Makarov DE, Makri N. Path integrals for dissipative systems by tensor multiplication. Condensed phase quantum dynamics for arbitrarily long time. *Chemical physics letters*. 1994;221(5-6):482-91.
- ²⁰Su Y, Chen ZH, Wang Y, Zheng X, Xu RX, Yan Y. Extended dissipaton equation of motion for electronic open quantum systems: Application to the Kondo impurity model. *The Journal of Chemical Physics*. 2023;159(2).
- ²¹Yan Y, Xu M, Li T, Shi Q. Efficient propagation of the hierarchical equations of motion using the Tucker and hierarchical Tucker

- tensors. *The Journal of Chemical Physics*. 2021;154(19).
- ²²Gong H, Ullah A, Ye L, Zheng X, Yan Y. Quantum entanglement of parallel-coupled double quantum dots: A theoretical study using the hierarchical equations of motion approach. *Chinese Journal of Chemical Physics*. 2018;31(4):510.
- ²³Xu M, Yan Y, Shi Q, Ankerhold J, Stockburger J. Taming quantum noise for efficient low temperature simulations of open quantum systems. *Physical Review Letters*. 2022;129(23):230601.
- ²⁴Bai S, Zhang S, Huang C, Shi Q. Hierarchical Equations of Motion for Quantum Chemical Dynamics: Recent Methodology Developments and Applications. *Accounts of Chemical Research*. 2024;57(21):3151-60.
- ²⁵Wang Y, Mulvihill E, Hu Z, Lyu N, Shivpuje S, Liu Y, et al. Simulating open quantum system dynamics on NISQ computers with generalized quantum master equations. *Journal of Chemical Theory and Computation*. 2023;19(15):4851-62.
- ²⁶Makri N. Quantum Dynamics Methods Based on the Real-Time Path Integral. In: *Comprehensive Computational Chemistry*, First Edition: Volume 1-4. Elsevier; 2023. p. V4-293.
- ²⁷Han L, Chernyak V, Yan YA, Zheng X, Yan Y. Stochastic Representation of Non-Markovian Fermionic Quantum Dissipation. *Physical review letters*. 2019;123(5):050601.
- ²⁸Han L, Ullah A, Yan YA, Zheng X, Yan Y, Chernyak V. Stochastic equation of motion approach to fermionic dissipative dynamics. I. Formalism. *The Journal of Chemical Physics*. 2020;152(20):204105.
- ²⁹Ullah A, Han L, Yan YA, Zheng X, Yan Y, Chernyak V. Stochastic equation of motion approach to fermionic dissipative dynamics. II. Numerical implementation. *The Journal of Chemical Physics*. 2020;152(20):204106.
- ³⁰Chen L, Bennett DI, Eisfeld A. Simulation of absorption spectra of molecular aggregates: A hierarchy of stochastic pure state approach. *The Journal of Chemical Physics*. 2022;156(12).
- ³¹Dan X, Xu M, Yan Y, Shi Q. Generalized master equation for charge transport in a molecular junction: Exact memory kernels and their high order expansion. *The Journal of Chemical Physics*. 2022;156(13).
- ³²Stockburger JT. Exact propagation of open quantum systems in a system-reservoir context. *EPL (Europhysics Letters)*. 2016;115(4):40010.
- ³³Lyu N, Mulvihill E, Soley MB, Geva E, Batista VS. Tensor-train thermo-field memory kernels for generalized quantum master equations. *Journal of Chemical Theory and Computation*. 2023;19(4):1111-29.
- ³⁴Liu Y, Yan Y, Xu M, Song K, Shi Q. Exact generator and its high order expansions in time-convolutionless generalized master equation: Applications to spin-boson model and excitation energy transfer. *Chinese Journal of Chemical Physics*. 2018;31(4):575-83.
- ³⁵Schmidt JR, Parandekar PV, Tully JC. Mixed quantum-classical equilibrium: Surface hopping. *J Chem Phys*. 2008;129(4):044104.
- ³⁶Amati G, Runeson JE, Richardson JO. On detailed balance in nonadiabatic dynamics: From spin spheres to equilibrium ellipsoids. *J Chem Phys*. 2023;158:064113.
- ³⁷Amati G, Mannouch JR, Richardson JO. Detailed balance in mixed quantum-classical mapping approaches. *J Chem Phys*. 2023;159:214114.
- ³⁸Mannouch JR, Kelly A. Toward a Correct Description of Initial Electronic Coherence in Nonadiabatic Dynamics Simulations. *J Phys Chem Lett*. 2024;15:11687-95.
- ³⁹Ullah A, Richardson JO. Machine learning meets su (n) Lie algebra: Enhancing quantum dynamics learning with exact trace conservation. *The Journal of Chemical Physics*. 2025;162(24):244106.
- ⁴⁰Ullah A, Dral PO. Speeding up quantum dissipative dynamics of open systems with kernel methods. *New Journal of Physics*. 2021.
- ⁴¹Ullah A, Dral PO. Predicting the future of excitation energy transfer in light-harvesting complex with artificial intelligence-based quantum dynamics. *Nature communications*. 2022;13(1930):1-8.
- ⁴²Ullah A, Dral PO. One-Shot Trajectory Learning of Open Quantum Systems Dynamics. *The Journal of Physical Chemistry Letters*. 2022;13(26):6037-41.
- ⁴³Rodríguez LEH, Ullah A, Espinosa KJR, Dral PO, Kananenka AA. A comparative study of different machine learning methods for dissipative quantum dynamics. *Machine Learning: Science and Technology*. 2022;3(4):045016.
- ⁴⁴Herrera Rodríguez LE, Kananenka AA. Convolutional neural networks for long time dissipative quantum dynamics. *The Journal of Physical Chemistry Letters*. 2021;12(9):2476-83.
- ⁴⁵Ge F, Zhang L, Hou YF, Chen Y, Ullah A, Dral PO. Four-dimensional-spacetime atomistic artificial intelligence models. *The Journal of Physical Chemistry Letters*. 2023;14(34):7732-43.
- ⁴⁶Zhang L, Ullah A, Pinheiro Jr M, Dral PO, Barbatti M. Excited-state dynamics with machine learning. In: *Quantum Chemistry in the Age of Machine Learning*. Elsevier; 2023. p. 329-53.
- ⁴⁷Wu D, Hu Z, Li J, Sun X. Forecasting nonadiabatic dynamics using hybrid convolutional neural network/long short-term memory network. *The Journal of Chemical Physics*. 2021;155(22):224104.
- ⁴⁸Lin K, Peng J, Xu C, Gu FL, Lan Z. Automatic evolution of machine-learning-based quantum dynamics with uncertainty analysis. *Journal of Chemical Theory and Computation*. 2022;18(10):5837-55.
- ⁴⁹Bandyopadhyay S, Huang Z, Sun K, Zhao Y. Applications of neural networks to the simulation of dynamics of open quantum systems. *Chemical Physics*. 2018;515:272-8.
- ⁵⁰Yang B, He B, Wan J, Kubal S, Zhao Y. Applications of neural networks to dynamics simulation of Landau-Zener transitions. *Chemical Physics*. 2020;528:110509.
- ⁵¹Lin K, Peng J, Xu C, Gu FL, Lan Z. Trajectory Propagation of Symmetrical Quasi-classical Dynamics with Meyer-Miller Mapping Hamiltonian Using Machine Learning. *The Journal of Physical Chemistry Letters*. 2022;13:11678-88.
- ⁵²Tang D, Jia L, Shen L, Fang WH. Fewest-Switches Surface Hopping with Long Short-Term Memory Networks. *The Journal of Physical Chemistry Letters*. 2022;13(44):10377-87.
- ⁵³Shakiba M, Philips AB, Autschbach J, Akimov AV. Machine Learning Mapping Approach for Computing Spin Relaxation Dynamics. *The Journal of Physical Chemistry Letters*. 2024. In press.
- ⁵⁴Lin K, Gao X. Enhancing Open Quantum Dynamics Simulations Using Neural Network-Based Non-Markovian Stochastic Schrödinger Equation Method. *arXiv preprint arXiv:241115914*. 2024.
- ⁵⁵Zeng H, Kou Y, Sun X. How Sophisticated Are Neural Networks Needed to Predict Long-Term Nonadiabatic Dynamics? *Journal of Chemical Theory and Computation*. 2024;20(22):9832-48.
- ⁵⁶Long C, Cao L, Ge L, Li QX, Yan Y, Xu RX, et al. Quantum neural network approach to Markovian dissipative dynamics of many-body open quantum systems. *The Journal of Chemical Physics*. 2024;08:161(8):084105. Available from: <https://doi.org/10.1063/5.0220357>.
- ⁵⁷Cao L, Ge L, Zhang D, Li X, Wang Y, Xu RX, et al. Neural Network Approach for Non-Markovian Dissipative Dynamics of Many-Body Open Quantum Systems. *arXiv preprint arXiv:240411093*. 2024.
- ⁵⁸Zhang J, Chen L. A non-Markovian neural quantum propagator and its application in the simulation of ultrafast nonlinear spectra. *Phys Chem Chem Phys*. 2025;27:182-9. Available from: <http://dx.doi.org/10.1039/D4CP03736G>.
- ⁵⁹Zhang J, Benavides-Riveros CL, Chen L. Artificial-Intelligence-Based Surrogate Solution of Dissipative Quantum Dynamics: Physics-Informed Reconstruction of the Universal Propagator. *The Journal of Physical Chemistry Letters*. 2024;15(13):3603-10.
- ⁶⁰Herrera Rodríguez LE, Kananenka AA. A short trajectory is all you need: A transformer-based model for long-time dissipative quantum dynamics. *The Journal of Chemical Physics*. 2024;161(17).

- ⁶¹Ullah A, Dral PO. MLQD: A package for machine learning-based quantum dissipative dynamics. *Computer Physics Communications*. 2024;294:108940.
- ⁶²Zhang J, Benavides-Riveros CL, Chen L. Neural quantum propagators for driven-dissipative quantum dynamics. *Phys Rev Res*. 2025 Jan;7:L012013. Available from: <https://link.aps.org/doi/10.1103/PhysRevResearch.7.L012013>.
- ⁶³Ullah A. From short-sighted to far-sighted: A comparative study of recursive machine learning approaches for open quantum systems. *Communications in Computational Chemistry*. 2025;7(3):209.
- ⁶⁴Zhang J, Benavides-Riveros CL, Chen L. Neural network solution of non-Markovian quantum state diffusion and operator construction of quantum stochastic process. *The Journal of Chemical Physics*. 2025;163(19):194103.
- ⁶⁵Zhao SC, Huang YM, Yang YF, Zhao ZR. Multi-Time-Scale Time Encoding for CNN Prediction of Fenna–Matthews–Olson Energy-Transfer Dynamics. *The Journal of Physical Chemistry Letters*. 2025;16:12820-7.
- ⁶⁶Renou MO, Trillo D, Weilenmann M, Le TP, Tavakoli A, Gisin N, et al. Quantum theory based on real numbers can be experimentally falsified. *Nature*. 2021;600(7890):625-9.
- ⁶⁷Chen MC, Wang C, Liu FM, Wang JW, Ying C, Shang ZX, et al. Ruling out real-valued standard formalism of quantum theory. *Physical Review Letters*. 2022;128(4):040403.
- ⁶⁸Li ZD, Mao YL, Weilenmann M, Tavakoli A, Chen H, Feng L, et al. Testing real quantum theory in an optical quantum network. *Physical Review Letters*. 2022;128(4):040402.
- ⁶⁹Wang F, Wang G, Zhang Y, Wang S, Li W, Huang B, et al. iFairy: the First 2-bit Complex LLM with All Parameters in $\{\pm 1, \pm i\}$. arXiv preprint arXiv:250805571. 2025.
- ⁷⁰Cole E, Cheng J, Pauly J, Vasanawala S. Analysis of deep complex-valued convolutional neural networks for MRI reconstruction and phase-focused applications. *Magnetic resonance in medicine*. 2021;86(2):1093-109.
- ⁷¹Igelnik B, Tabib-Azar M, Pao YH, LeClair S. A quantum neural net: with applications to materials science. In: Proceedings of the Second International Conference on Intelligent Processing and Manufacturing of Materials. IPMM'99 (Cat. No. 99EX296). vol. 1. IEEE; 1999. p. 367-74.
- ⁷²Trabelsi C, Bilaniuk O, Zhang Y, Serdyuk D, Subramanian S, Santos JF, et al. Deep Complex Networks. In: International Conference on Learning Representations; 2018. .
- ⁷³Bassey J, Qian L, Li X. A survey of complex-valued neural networks. arXiv preprint arXiv:210112249. 2021.
- ⁷⁴Zhang L, Du M, Bai X, Chen Y, Zhang D. Complex-valued physics-informed machine learning for efficient solving of quintic nonlinear Schrödinger equations. *Physical Review Research*. 2025;7(1):013164.
- ⁷⁵Dong YC, Li XK, Yang M, Lu Y, Liao YL, Ullah A, et al. Quantum state classification via complex-valued neural networks. *Laser Physics Letters*. 2024;21(10):105206.
- ⁷⁶Barrachina JA, Ren C, Morisseau C, Vieillard G, Ovarlez JP. Complex-valued vs. real-valued neural networks for classification perspectives: An example on non-circular data. In: ICASSP 2021-2021 IEEE International Conference on Acoustics, Speech and Signal Processing (ICASSP). IEEE; 2021. p. 2990-4.
- ⁷⁷Yang B, Zhang W, Gong LN, Ma HZ. Finance time series prediction using complex-valued flexible neural tree model. In: 2017 13th International Conference on Natural Computation, Fuzzy Systems and Knowledge Discovery (ICNC-FSKD). IEEE; 2017. p. 54-8.
- ⁷⁸He K, Zhang X, Ren S, Sun J. Delving Deep into Rectifiers: Surpassing Human-Level Performance on ImageNet Classification. In: 2015 IEEE International Conference on Computer Vision (ICCV); 2015. p. 1026-34.
- ⁷⁹Ullah A, Rodríguez LEH, Dral PO, Kananenka AA. QD3SET-1: A Database with Quantum Dissipative Dynamics Data Sets. *Frontiers in Physics*. 2023;11:1223973.
- ⁸⁰Shi Q, Chen L, Nan G, Xu RX, Yan Y. Efficient hierarchical Liouville space propagator to quantum dissipative dynamics. *The Journal of chemical physics*. 2009;130(8):084105.
- ⁸¹Chen ZH, Wang Y, Zheng X, Xu RX, Yan Y. Universal time-domain Prony fitting decomposition for optimized hierarchical quantum master equations. *The Journal of Chemical Physics*. 2022;156:221102.
- ⁸²Mohseni M, Rebentrost P, Lloyd S, Aspuru-Guzik A. Environment-assisted quantum walks in photosynthetic energy transfer. *J Chem Phys*. 2008;129(17):11B603.
- ⁸³Adolphs J, Renger T. How proteins trigger excitation energy transfer in the FMO complex of green sulfur bacteria. *Biophysical journal*. 2006;91(8):2778-97.
- ⁸⁴Jia X, Mei Y, Zhang JZ, Mo Y. Hybrid QM/MM study of FMO complex with polarized protein-specific charge. *Scientific reports*. 2015;5(1):17096.
- ⁸⁵Dral PO. MLatom: A program package for quantum chemical research assisted by machine learning. *Journal of computational chemistry*. 2019;40(26):2339-47.

Supporting Information
 for
Toward Quantum-Aware Machine Learning: Improved Prediction of Quantum Dissipative Dynamics via Complex Valued Neural Networks

Muhammad Atif, Arif Ullah,* and Ming Yang†
School of Physics, Anhui University, Hefei 230601, China
 (Dated: January 8, 2026)

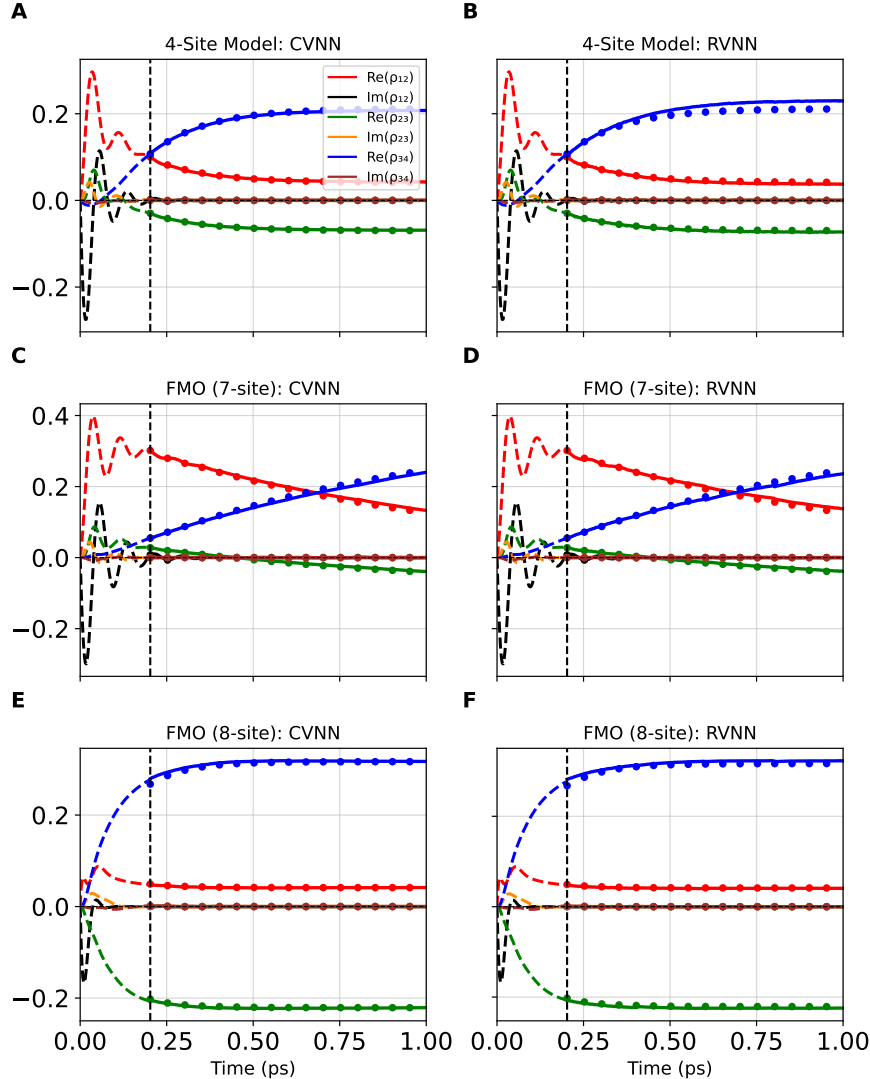


FIG. S1. Time evolution of selected prominent RDM off-diagonal (coherence) terms predicted by CVNN and RVNN models. Each row corresponds to an FMO complex: 4-site (A, B), 7-site (C, D), and 8-site (E, F). The left column (A, C, E) displays CVNN predictions; the right column (B, D, F) displays RVNN predictions. Reference dynamics are overlaid as dots. A vertical dashed line in each panel separates the provided input dynamics from the predicted dynamics. Parameters: 4-site ($\gamma = 250 \text{ cm}^{-1}$, $\lambda = 70 \text{ cm}^{-1}$, $T = 130 \text{ K}$); 7-site ($\gamma = 350 \text{ cm}^{-1}$, $\lambda = 70 \text{ cm}^{-1}$, $T = 30 \text{ K}$); 8-site ($\gamma = 400 \text{ cm}^{-1}$, $\lambda = 250 \text{ cm}^{-1}$, $T = 30 \text{ K}$).

* arif@ahu.edu.cn

† mingyang@ahu.edu.cn